

Fundamental performance bounds on time-series generation using reservoir computing

Daoyuan Qian¹ and Ila Fiete^{2,3,†}

¹*Centre for Misfolding Diseases, Yusuf Hamied Department of Chemistry, University of Cambridge, Lensfield Road, Cambridge CB2 1EW, U.K.*

²*McGovern Institute for Brain Research, Massachusetts Institute of Technology, MA 02139, U.S.A.*

³*Department of Brain and Cognitive Sciences, Massachusetts Institute of Technology, MA 02139, U.S.A.*

(Dated: October 29, 2024)

Reservoir computing (RC) harnesses the intrinsic dynamics of a chaotic system, called the reservoir, to perform various time-varying functions. An important use-case of RC is the generation of target temporal sequences via a trainable output-to-reservoir feedback loop. Despite the promise of RC in various domains, we lack a theory of performance bounds on RC systems. Here, we formulate an existence condition for a feedback loop that produces the target sequence. We next demonstrate that, given a sufficiently chaotic neural network reservoir, two separate factors are needed for successful training: global network stability of the target orbit, and the ability of the training algorithm to drive the system close enough to the target, which we term ‘reach’. By computing the training phase diagram over a range of target output amplitudes and periods, we verify that reach-limited failures depend on the training algorithm while stability-limited failures are invariant across different algorithms. Finally, we leverage dynamical mean field theory (DMFT) to provide an analytical amplitude-period bound on achievable outputs by RC networks and propose a way of enhancing algorithm reach via forgetting. The resulting mechanistic understanding of RC performance can guide the future design and deployment of reservoir networks.

I. INTRODUCTION

Random neural networks with strong connectivity generically exhibit chaotic dynamics [1, 2]. The reservoir computing (RC) paradigm seeks to functionalise the dynamics of such networks by treating the neural firing rates as a source (reservoir) of temporal basis functions which can be combined through a linear layer to produce an output of desired properties [3, 4]. Time-series generation is an important and natural application of RC, where training the final output layer leads to rapid convergence of the output towards a given target function, provided that the network is stabilised by a fixed feedback loop [5]. The appeal of RC over conventional machine learning models for time series is that while the outputs and feedback into the reservoir are optimised by training, the reservoir remains intact, so the training process can be significantly more efficient [6]. Reservoirs can be instantiated as physical systems, with examples including coupled mechanical [7] or chemical oscillators [8], electronic circuits [9], photonic systems [10], and quantum computers [11].

Typically, the readout parameters from the reservoir are trained using the recursive least-squares (RLS) method [12]. During training, either the network’s current output or the target output is fed back to the system, giving rise to the first-order reduced and controlled error (FORCE) [5] algorithm and the echo state [13] algorithm, respectively. Training is successful if the output remains close to the target after the readout parameters are fixed. In the brain, it is hypothesised that the sequence-learning

ability of random networks may underlie the generation of motor movement sequences in the cortex [5]. Computational models further illustrate how low-rank perturbative feedback (from the cortex via the thalamus) to a reservoir (cortex) can stabilize and combine multiple output trajectories to generate complex motor sequences [14].

While past work has focused on various applications of RC across domains, we understand little about the bounds on performance using RC and when and why training may succeed or fail. In general, successful learning of a target function depends on multiple factors: first (existence condition), a dynamical orbit that produces the target function must exist; second (stability condition), this orbit needs to be stable over time; and third (reach condition), the training algorithm has to be able to reach this orbit during training. In this work, we examine each condition using a combination of analytical theory and numerical simulations, leading to rules that determine whether an RC implementation of a time-series generation task can be successful.

We find that the existence condition depends on network size and is easily satisfied for a large reservoir, but the orbit stability and the reach of the algorithm play major roles in determining which functions can be learned. To understand the latter factors, we train a network to produce sinusoidal waves of a range of amplitude A and period T , and compute the relative training error in the $A - T$ space. We derive a stability-related phase boundary using a dynamical mean-field theory (DMFT) approach and verify its validity in simulations, and further show that a training algorithm can be tuned to achieve greater reach in the stable region. Taken together, our work illuminates distinct mechanisms that bound the performance of an RC reservoir, allowing for

† fiete@mit.edu

more informed implementation and optimisation of these systems.

II. RANDOM NEURAL NETWORK RESERVOIR COMPUTER

We take as the reservoir a network of N randomly connected neurons labeled by index $i = 1, 2, \dots, N$. The neural membrane potential and firing rate at time t are denoted $h_i(t)$ and $r_i(t)$ respectively. They are related via $r_i(t) = \phi[h_i(t)]$, where in numerical computations the non-linearity $\phi(\cdot)$ is taken to be $\phi(\cdot) \equiv \tanh(\cdot)$. The dynamical equation is

$$\frac{d}{dt}h_i(t) = -\frac{1}{\tau}h_i(t) + g \sum_{j=1}^N J_{ij}r_j(t) + I_i(t), \quad (1)$$

where τ is the decay time of the membrane potential of individual neurons, J_{ij} is a random connectivity matrix satisfying $\langle J_{ij} \rangle = 0$ and $\langle J_{ij}^2 \rangle = \frac{1}{N}$, g sets the connection strength, and $I_i(t)$ is an external input into the i -th neuron. When $g > \frac{1}{\tau}$ and in the absence of external input, the potentials exhibit chaotic dynamics [1]. The RC output $z(t)$ is the weighted sum of all reservoir neuron firing rates, and is fed back to the system via a feedback vector K_i :

$$z(t) \equiv \sum_{i=1}^N w_i r_i(t), \quad I_i(t) \equiv K_i z(t). \quad (2)$$

The readout weights w_i are trained while the recurrent and feedback weights J_{ij} and K_i remain fixed (Figure 1). The aim of training is to find a w_i such that $z(t)$ mimics the target sequence $f(t)$, where $f(t)$ can take complicated forms.

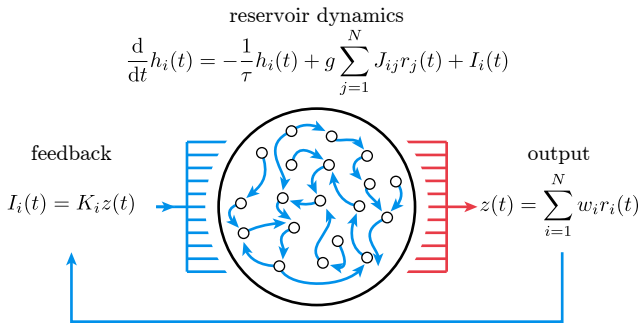


FIG. 1. **Implementing RC with a random neural network.** A reservoir of N neurons is recurrently coupled via a random matrix J_{ij} . The RC output is a weighted sum of reservoir firing rates $r_i(t)$. A feedback loop re-injects the output into the reservoir, to push it toward a stable limit cycle. Only the output weights w_i are trained (red lines), while the recurrent and feedback weights K_i are fixed (blue lines).

III. EXISTENCE OF A SOLUTION

Least-squared minimisation of the integrated quadratic error leads to an expression for the weight vector required to solve the task [5]:

$$w_i = \sum_{j=1}^N P_{ij} \int r_j(t) f(t) dt, \quad (3)$$

where P_{ij} is the regularised inverse coorelation matrix

$$P_{ij} \equiv \left(R_{ij} + \frac{1}{\alpha} \delta_{ij} \right)^{-1}, \quad R_{ij} \equiv \int r_i(t) r_j(t) dt. \quad (4)$$

The regularizer α is added to avoid numerical issues with matrix inversion. Substituting Eq. (3) into the first of Eq. (2) gives the output of the RC network as

$$z(t) = (D * f)(t), \quad D(t, t') = \sum_{i,j=1}^N r_i(t) P_{ij} r_j(t'), \quad (5)$$

where $*$ denotes a convolution. Thus, the existence of an orbit in the RC dynamics that reproduces the target requires that $D(t, t') \approx \delta(t - t')$. For a free network, without feedback or the regularizer, $D(t, t')$ behaves as a normalised Gaussian with effective variable $t - t'$ if the time horizon T (the length of the target sequence) is short enough, $T < N\tau_0$, where τ_0 is the auto-correlation time of a single neuron firing rate (Appendix A1). When R_{ij} is full-rank, we can remove the regulariser from Eq. (4) and the peak takes the value $\langle D(t, t') \rangle \approx \frac{N}{T}$, where the average is taken over t . However, if T is too short (compared to $N\tau_1$ where τ_1 is a de-correlation timescale, Appendix A1), R_{ij} becomes low-rank and a regulariser is needed to compute P_{ij} . With the regulariser, the peak in $D(t, t')$ is now (Appendix A2)

$$\langle D(t, t') \rangle \approx \frac{Np}{T}, \quad (6)$$

where p is the fraction of eigenvalues of R_{ij} significantly larger than $\frac{1}{\alpha}$. The peak width of $D(t, t')$ is thus $\frac{T}{Np}$. In practice, Np depends on the reservoir parameters, the regularizer, as well as the target function that drives the network via the feedback loop. For a good RC fit to a target, we would ideally have the width $\frac{T}{Np}$ to be much smaller than the fitting time horizon $T \gg \frac{T}{Np}$, so the condition for a successful RC implementation is that the relative smearing width is much less than 1, $1/Np \ll 1$. Furthermore, if we take $1/Np$ as a proxy for the fitting error denoted by η , we arrive at a scaling law for η with N , assuming p is constant:

$$\eta \sim \frac{1}{Np} \propto \frac{1}{N}. \quad (7)$$

This scaling is observed in numerical simulations of FORCE learning at different N , in the region of optimal training (Appendix B). In sum, the existence condition can be satisfied by sufficiently large reservoirs.

IV. STABILITY CONDITION: DMFT AND NUMERICAL VERIFICATION

After the weight vector w_i has been learned and weight updates have stopped, the network orbit must be stable. To analytically derive a stability condition for the dynamics, we set $f(t)$ to be a sinusoidal wave of amplitude A , period T , and angular frequency $\omega \equiv \frac{2\pi}{T}$:

$$f(t) = A \sin \omega t. \quad (8)$$

Letting $K_i = 1$ for now, by DMFT the mean membrane potential $\bar{h}(t)$ evolves as $\frac{d}{dt}\bar{h}(t) = -\frac{1}{\tau}\bar{h}(t) + A \sin \omega t$ [15], so that

$$\bar{h}(t) = \frac{A}{\sqrt{1/\tau^2 + \omega^2}} \sin(\omega t + \theta), \quad (9)$$

for some phase factor θ . When the network is perturbed from the ideal orbit by $\delta h_i(t)$, the equation governing its evolution is given by the perturbation of Eq. (1)

$$\frac{d}{dt}\delta h_i(t) = -\frac{1}{\tau}\delta h_i(t) + g \sum_j J_{ij} [1 - r_j^2(t)] \delta h_j(t). \quad (10)$$

Recall that $r_j(t) \subset [-1, 1]$, the eigenvalues of J_{ij} have a maximum magnitude of approximately 1, and $g > \frac{1}{\tau}$. Exponential growth of $\delta h_j(t)$ can be expected when $r_j(t) \approx 0$, and the perturbation shrinks when $r_j(t) \approx \pm 1$. The boundary between a stable and an unstable network is when the growth and decay of $\delta h_i(t)$ over one period exactly cancel each other. To quantify this statement, we make the mean-field replacement

$$r_j(t) \approx \tanh \bar{h}(t), \quad (11)$$

and since the initial perturbation $\delta h_i(0)$ is arbitrary, we focus on the eigenvector of J_{ij} with the largest real eigenvalue, of order 1. The reduced model is then, upon rearrangement and dropping the subscript for brevity,

$$\frac{d}{dt} \ln \delta h(t) = -\frac{1}{\tau} + g [1 - \tanh^2 \bar{h}(t)]. \quad (12)$$

Network stability is given by the time integral of the right hand side, with positive and negative values indicating unstable and stable orbits respectively. Since \bar{h} is given explicitly by Eq. (9), the instability boundary satisfies

$$\int_{-\infty}^{\infty} dt' \left\{ -\frac{1}{\tau} + g \left[1 - \tanh^2 \left(\frac{A}{\sqrt{1/\tau^2 + \omega^2}} \sin t' \right) \right] \right\} = 0. \quad (13)$$

In the above we have re-scaled and shifted the dummy time variable by $t' \equiv \omega t + \theta$ such that the parameters A and ω appear in a combined form $A/\sqrt{1/\tau^2 + \omega^2}$. As a result, when both τ and g are fixed, the stable-unstable boundary on an $A - \omega$ plot should follow

$$A \propto \sqrt{\frac{1}{\tau^2} + \omega^2}. \quad (14)$$

Because $T = 2\pi/\omega$, we expect the success/failure boundary in $A - T$ space to have the scaling $A \propto T^{-1}$ when the period T is much smaller than τ , and plateaus when T becomes larger than τ . If $f(t)$ is composed of a few sinusoidal waves, the mean potential Eq. (9) acquires additional terms of the form $A/\sqrt{1/\tau^2 + n^2\omega^2}$ for some integer n (Appendix C). The T^{-1} scaling still holds for small T . Interestingly, Eq. (14) implies that in the subchaotic regime of $\frac{1}{\tau} > g$, all orbits should be stable.

V. REACH OF THE LEARNING ALGORITHM

The existence of a stable solution orbit does not necessarily imply that a learning algorithm can reach it. To understand the contribution of learning algorithms, we first outline the RLS update scheme [12], used in both FORCE and echo learning [5, 13]. The weight vector w_i and inverse correlation matrix P_{ij} are kept in memory and updated at time intervals Δt . Using the shorthand $\mathbf{P}_0 \equiv P_{ij}(0)$, $\mathbf{w}_0 \equiv w_j(0)$, $\mathbf{P} \equiv P_{ij}(t)$, $\mathbf{w} \equiv w_j(t)$, $\mathbf{r} \equiv r_j(t)$, $\mathbf{P}' \equiv P_{ij}(t + \Delta t)$, $\mathbf{w}' \equiv w_j(t + \Delta t)$, and $\mathbf{r}' \equiv r_j(t + \Delta t)$, the RLS algorithm is

$$\begin{aligned} \mathbf{P}_0 &= \alpha \mathbf{1}, \quad \mathbf{w}_0 = \mathbf{0}, \\ \mathbf{P}' &= \mathbf{P} - \frac{\mathbf{P} \mathbf{r}' \mathbf{r}'^T \mathbf{P}}{1 + \mathbf{r}'^T \mathbf{P} \mathbf{r}'}, \\ \mathbf{w}' &= \mathbf{w} - \mathbf{P}' \mathbf{r}' e', \end{aligned} \quad (15)$$

where $e' \equiv z(t + \Delta t) - f(t + \Delta t)$ is the instantaneous error at $t + \Delta t$. In essence, the RLS algorithm performs the integrals in Eqs. (3) and (4) on the fly. The difference between FORCE and echo learning is that during training in FORCE learning, the feedback is set to $I_i(t) = K_i z(t)$, while in echo learning it is $I_i(t) = K_i f(t)$. Feeding the network its own output allows system fluctuations to be corrected during training, leading to better performance in finding the ideal orbit [5]. A side effect of allowing the feedback to fluctuate in FORCE learning is that the firing rates $r_i(t)$ can deviate from the ideal orbit, and as such the inverse correlation matrix becomes corrupted by fluctuations. Furthermore, a large α in principle reduces the overall error, however setting α to be large at initialisation leads to numerical instabilities. To address these limitations we formulate a new training algorithm, forgetful FORCE, which introduces a forgetting step to remove fluctuation-driven corruption and anneals the system towards large α over time. Forgetful FORCE learning involves an intermediate matrix \mathbf{P}'' at each update step

$$\begin{aligned} \mathbf{P}'' &= \frac{1}{1 - \gamma} \mathbf{P}, \\ \mathbf{P}' &= \mathbf{P}'' - \frac{\mathbf{P}'' \mathbf{r}' \mathbf{r}'^T \mathbf{P}''}{1 + \mathbf{r}'^T \mathbf{P}'' \mathbf{r}'}, \end{aligned} \quad (16)$$

with a forgetting parameter γ . This is equivalent to multiplying the correlation matrix R_{ij} by a factor $(1 - \gamma)$ before each update, and the system retains a memory of its

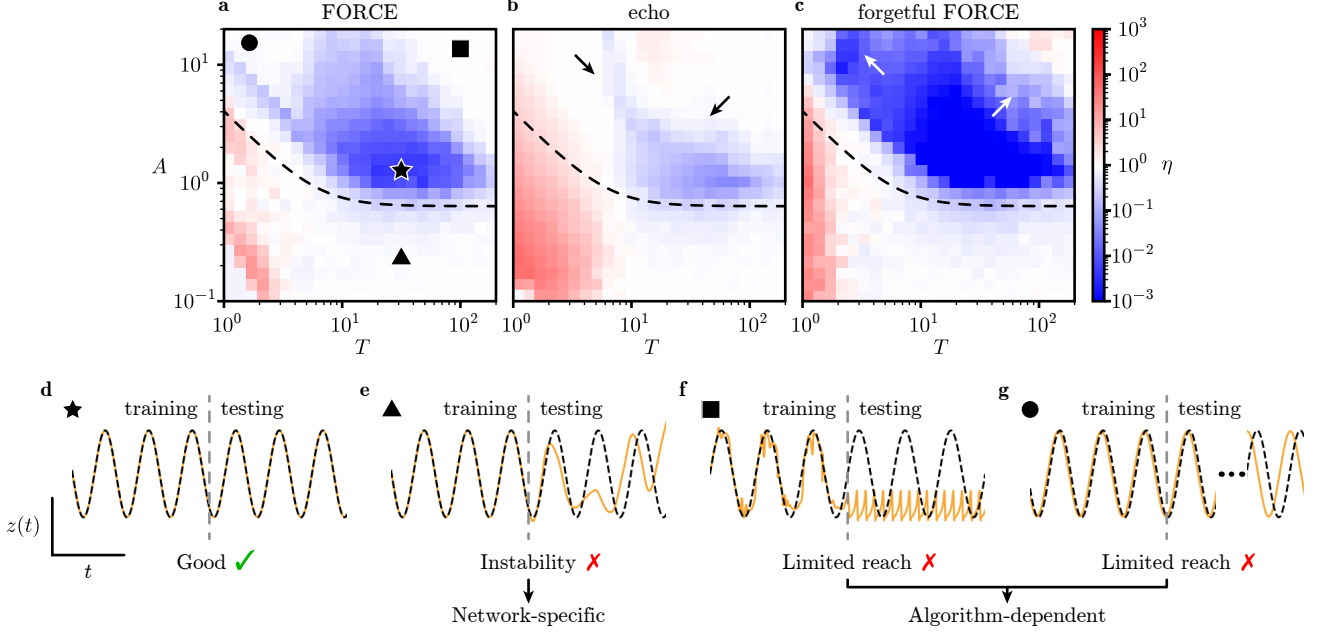


FIG. 2. **Probing performance bounds on RC by training on sinusoidal waves.** We compare training phase diagrams of three different algorithms: **a** FORCE learning from [5], **b** echo learning, and **c** learning with a forgetting parameter $\gamma = 0.002$. Black dashed lines are instability-induced failure phase boundaries from Eq. (14), and the dark blue (success) regions do not extend beyond this boundary in all three cases. Echo learning is less expressive (black arrows indicating shrinkage of the blue region), while forgetful FORCE enlarges the blue region (white arrows). Examining the output traces from FORCE simulations show different types of failure. In **d-g**, orange lines are the network output and black dashed lines are the target output. **d** In the success region, the output and target overlap during and after training. **e** If the target function is outside the stable region, the output matches the target during training but drifts away from it during testing. **f, g** Within the stable regime, the network can still fail to learn the target function due to limited algorithm reach, and these failures are characterised by output-target mismatches both during and after training.

past only over the timescale $\Delta t/\gamma$. Forgetting should improve algorithm reach in regions where a stable solution exists, but should not affect instability-induced failure.

VI. NUMERICAL VERIFICATIONS

We test the performance of FORCE, echo, and forgetful FORCE algorithms by training a random neural network to produce the sinusoidal wave as in Eq. (8). We use typical RC parameters [5] $\tau = 1$, $g = 1.5$, $N = 1000$, $\Delta t = 0.1$, $\alpha = 1$, an integration time step $dt = 0.01$, and draw K_i uniformly and independently from the interval $(-1, 1)$. The training phase is simulated for 400 time units, after which a testing phase ensues with the weight w_i fixed for another 400 time units. Simulating the training phase with 200 or 600 time units does not show significant differences to 400 time units. We perform a parameter sweep over A and T , and 20 different network realisations are simulated at each parameter combination. We quantify the success or failure of a training episode by computing the relative error η in the

testing phase with fixed w_i

$$\eta \equiv \sqrt{\langle [f(t) - z(t)]^2 \rangle} / A, \quad (17)$$

where the average is taken over time t . η is then equivalent to the noise-to-signal ratio, and successful training should lead to $\eta \ll 1$.

Computing the average η for a range of A and T for all three training algorithms indeed confirms our results pertaining to stability and reach. In the low- T (high- ω) regime, the FORCE boundary exhibits the predicted scaling relation $A \propto T^{-1}$ that plateaus at higher T (Figure 2a, dashed black line). Regardless of learning rule — FORCE (Figure 2a), echo (Figure 2b), or forgetful FORCE (Figure 2c) — the empirical success region does not extend below this stability boundary. However, the algorithms differ from each other in the high- A , stable region. For the same reservoir parameter g , echo learning performs worse than FORCE since the feedback does not include network fluctuations, while forgetful FORCE has highest reach because it keeps only relevant correlation information and anneals away the regulariser. Examining network outputs for individual runs shows qualitative differences between instability and low-reach failures. For

a successful training run, the output matches the target both during and after training (Figure 2d). In the unstable region, the output matches the target during training but diverges from it when weight updates are stopped (Figure 2e). In the low-reach region, the output differs from the target both during and after training: the algorithm fails to reach the ideal orbit even during training (Figure 2f, 2g).

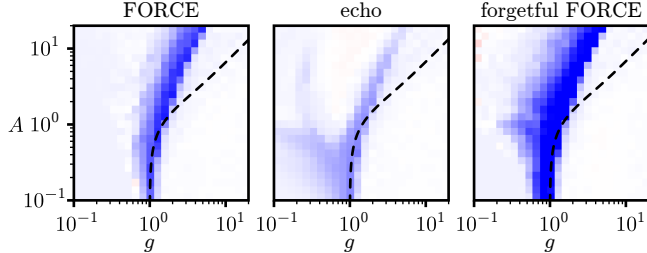


FIG. 3. $A - g$ parameter sweep reveals instability boundary near $g = 1$. Analytical DMFT result suggests the network should always be stable to the left of the black dashed lines. Simulations (blue) indeed show a sharp instability boundary that coincides at low amplitudes (boundary goes to $A \rightarrow 0$ with $g \rightarrow 1$). The deviation between the two at large g indicates a breakdown of DMFT due to the increased effect of fluctuations. In the stable regime, training can still fail in an algorithm-dependent manner, indicating varying degrees of training success among the three tested algorithms. The colour code follows that of Figure 2a - 2c.

The DMFT expression Eq. (13) also suggests that the network should always be stable in the subchaotic regime, $g < \frac{1}{\tau} = 1$. Sub-chaotic reservoirs have been observed to have worse performance in sequence learning [5], but the reasons are unclear. To gain more insight on how performance depends on g , we perform a parameter sweep of A against g , with $T = 30$ and all other parameters the same as before. All three algorithms exhibit a sharp success/failure boundary (Figure 3). For a significant region, this boundary is near $g = 1$, confirming our expectation that the chaotic regime is detrimental to network stability. We also numerically solved the analytical expression from Eq. (13) to compute the $A - g$ phase boundary (Figure 3, black dashed lines). Despite the deviation of the analytical $A - g$ curve from simulations for g away from criticality, they agree qualitatively. This indicates that first-order fluctuations in $r_j(t)$ can also depend on A and T in a combined form $A/\sqrt{1/\tau^2 + \omega^2}$, resulting in greater applicability of the $A - T$ boundary Eq. (14) than we had expected. The deviations at large g are possibly due to the de-stabilising effect of fluctuations omitted in the DMFT analysis. Future work could use a first-order approximation of $r_j(t)$ in addition to Eq. (11), although the analytical intractability of typical DMFT calculations means a simple closed-form solution is un-

likely, so we omit this in the current work. For $g < 1$, although the network should be stable at all A , the degree of training success varies among the algorithms (Figure 3), indicating that algorithm reach plays a more important role for sub-chaotic networks than the detailed value of g in this regime. Notably, algorithm reach deteriorates with decreasing g , and the best training quality can be achieved at $g \approx 1$, at the edge of chaos.

VII. CONCLUSION

In this work, we delineated two distinct factors that are required to successfully train a reservoir computing network with a large reservoir: dynamic stability and learning algorithm reach. The former is an intrinsic property of the network and can be understood using a DMFT approach. We demonstrate the effect of the latter via direct computation of training phase diagrams using three different training algorithms. The new theoretical understanding of RC also carries practical implications. We proposed a new training algorithm whose reach improves on that of existing algorithms by only taking into consideration recent trajectory data and with annealing of the regularisation term. Further, applying different training algorithms to a single system can potentially illuminate an algorithm-independent performance boundary, such that if the desired function falls outside this boundary then it is necessary to modify the reservoir itself. Making biological reservoirs using cultured neurons is also an area under active exploration [16] and experimentally measuring the stability boundary could provide a way to characterise an *in vitro* network using coarse-grained parameters that are typically employed in computational models. Separating network-specific and algorithm-dependent failures can be a new approach to study experimentally constructed RC systems and facilitate their development.

Conflict of interest The authors declare no conflict of interest.

Code availability The simulation scripts used in this work will be made available as a GitHub repository upon acceptance for publication.

Acknowledgement The study is funded by Transition Bio Ltd (D.Q.). IRF is supported in part by the Simons Foundation (SCGB program 1181110), the ONR (award N00014-19-1-2584), and the NSF (CISE award IIS-2151077 under the Robust Intelligence program). The authors thank Mr David Clark for insightful discussions.

Appendix A: Properties of the correlator $D(t, t')$

In this section, we use the summation convention where repeated indices are assumed to be summed unless stated otherwise.

1. Full rank random dynamics

In the absence of input currents, the firing rates $r_i(t)$ have no periodic structure. We are interested in the function

$$D(t, t') = r_i(t)P_{ij}r_j(t') \quad (\text{A1})$$

where P_{ij} is the inverse matrix of the integrated correlation

$$P_{ij} \int r_j(t)r_k(t)dt = \delta_{ik}. \quad (\text{A2})$$

We have omitted the regularizer for now. Integrating $D(t, t)$ over t leads to

$$\int D(t, t)dt = P_{ij}R_{ij} = \delta_{ii} = N, \quad \langle D(t, t) \rangle = \frac{N}{T}. \quad (\text{A3})$$

This is an exact result, and deviations from this can arise due to numerical issues with a large N or a small T , associated with an R_{ij} matrix of rank less than N . In particular, we can view $\{r_i(t) | 0 < t < T\}$ as a random sequence with a decorrelation time-scale of τ_1 , so effectively as a list of $\frac{T}{\tau_1}$ random numbers. τ_1 is not a network-specific timescale, as the decorrelation time-scale depends on the simulation hardware's ability to distinguish changes in $r_i(t)$, and thus only a numerical artefact. The full-rank condition for R_{ij} reads

$$N \lesssim \frac{T}{\tau_1}. \quad (\text{A4})$$

Eq. (A3) gives the peak height of $D(t - t') \equiv D(t, t')$. To provide intuition on why $D(t - t')$ should resemble a Dirac delta, we write $r_i(t)$ as a rectangular data matrix \mathbf{x} of dimension $\frac{T}{\delta t} \times N$, so $D(t, t')$ can be written as $\mathbf{D} = \mathbf{x}(\mathbf{x}^T \mathbf{x})^{-1} \mathbf{x}^T$. Furthermore, for a constant y

$$\begin{aligned} (\mathbf{x}^T \mathbf{x} + y\mathbf{I})\mathbf{x}^T &= \mathbf{x}^T(\mathbf{x}\mathbf{x}^T + y\mathbf{I}) \\ \mathbf{x}^T(\mathbf{x}\mathbf{x}^T + y\mathbf{I})^{-1} &= (\mathbf{x}^T \mathbf{x} + y\mathbf{I})^{-1} \mathbf{x}^T, \end{aligned} \quad (\text{A5})$$

and in the limit of $y \rightarrow 0^+$ these are the Moore-Penrose inverse of \mathbf{x} , denoted as \mathbf{x}^+ [17]:

$$\mathbf{x}^+ = \lim_{y \rightarrow 0^+} \mathbf{x}^T(\mathbf{x}\mathbf{x}^T + y\mathbf{I})^{-1} = \lim_{y \rightarrow 0^+} (\mathbf{x}^T \mathbf{x} + y\mathbf{I})^{-1} \mathbf{x}^T, \quad (\text{A6})$$

leading to

$$\mathbf{D} = \mathbf{x}(\mathbf{x}^T \mathbf{x})^{-1} \mathbf{x}^T = \mathbf{x}\mathbf{x}^+ \approx \mathbf{I}, \quad (\text{A7})$$

where \mathbf{I} in the last part is the identity matrix of dimension $\frac{T}{\delta t} \times \frac{T}{\delta t}$, which is a Dirac delta in the continuous picture. The approximation becomes equality if \mathbf{x} is invertible, however in practice the peak has a finite width. The mechanism becomes clear if we perform singular value decomposition on \mathbf{x} by writing $\mathbf{x} = \mathbf{U}\Sigma\mathbf{V}^T$ and $\mathbf{x}^+ = \mathbf{V}\Sigma^+\mathbf{U}^T$, where $\Sigma = \text{diag}(\lambda_1, \lambda_2, \dots, \lambda_N, 0, \dots, 0)$ with $\frac{T}{\delta t} - N$ zeros, and $\Sigma^+ = \text{diag}(1/\lambda_1, 1/\lambda_2, \dots, 1/\lambda_N, 0, \dots, 0)$. Then $\mathbf{x}\mathbf{x}^+ = \mathbf{U}\mathbf{I}^+\mathbf{U}^T$, with \mathbf{I}^+ comprising N 1's on the diagonal and the rest are 0. As a result, when $\frac{T}{\delta t} - N$ becomes large, more parts of \mathbf{U}^T are masked-out and the quality of the Dirac delta worsens. This continues until in the large- T regime, we can instead assume the neurons behave as independent units such that

$$\langle r_i(t)r_j(t') \rangle = \delta_{ij} \langle r^2 \rangle C(t - t'), \quad (\text{A8})$$

for a constant $\langle r^2 \rangle$ and a normalised single-site correlation satisfying $C(0) = 1$. It is straightforward to show, in this limit,

$$D(t - t') = \frac{N}{T} C(t - t'). \quad (\text{A9})$$

The integral over $(t - t')$ is now not normalised to 1 anymore but instead $N\tau_0/T$ for the single-site correlation time τ_0 . The transition occurs at $N\tau_0/T \approx 1$, or $T \approx N\tau_0$.

To test these results, we perform simulations of a free random network with 1000 neurones, and select $N = 100$ neurons to compute the $D(t - t')$ correlator. 1000 neurons are used in the actual simulation to produce chaotic activity. The peak height $D(0)$ agrees with Eq. (A3) for $T > N\tau_1 \approx 20$ (Figure 4 a). The integral $\int D(\delta t)d\delta t$ stays at 1 for $T < N\tau_0$ where $\tau_0 \approx 4$, beyond which the system resembles a reservoir of independent neurons (Figure 4 b). The $\tau_0 \approx 4$ also agrees with the typical correlation time of a random neural network [1, 15]. Examining individual $D(t - t')$ forms further shows that for small $T = 20$ and 200 , $D(t - t')$ are approximately normalised Gaussians as expected (Figure 5 a, left and mid), and becomes un-normalised for larger T (Figure 5 a, right). The standard deviation σ of the fitted Gaussian follows the theoretical predictions in both the small- T and large- T regime (Figure 5 b), where for large- T we explicitly compute $\int C(\delta t)d\delta t$ and use Eq. (A9) to get $\sigma \approx \frac{1}{\sqrt{2\pi}} \int C(\delta t)d\delta t$.

2. Correlator with a regularizer

For typical applications the network size N is large compared to the time horizon T normalised by τ_0 , $N \gg T/\tau_0$. In the stability study, we use $N = 1000$ and $T < 200$. In this regime, we expect $D(t, t + \delta t)$ to be normalised Gaussians. The practical problem with a large N relative to T is inversion of the correlation matrix R_{ij} .

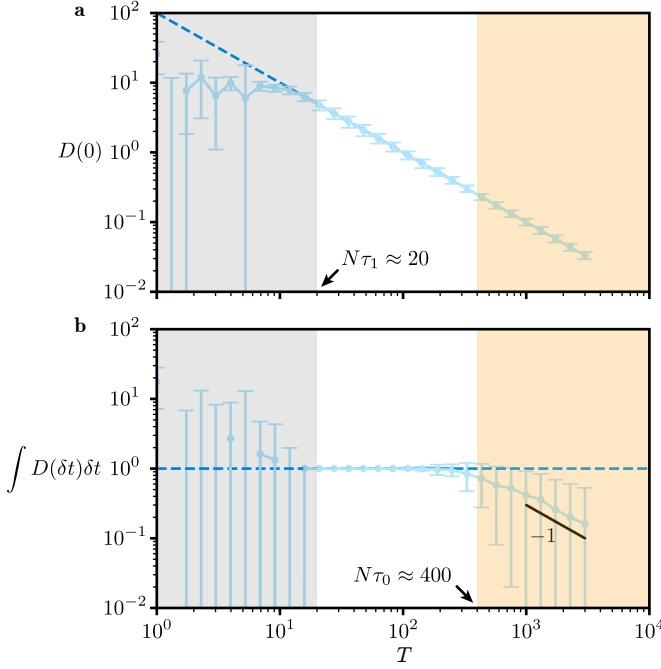


FIG. 4. **Properties of $D(t - t')$.** **a** $D(0)$ computed using $N = 100$ neurons (blue solid line) agrees with $\frac{N}{T}$ (blue dashed line) for $T > 20$, giving $\tau_1 \approx 0.2$. This is the timescale below which inversion of R_{ij} becomes numerically unstable (grey region). **b** Integral of $D(t - t')$ stays 1 for $N\tau_1 < T < N\tau_0$ where $\tau_0 \approx 4$. The independent neuron assumption becomes valid for large T (orange region), as indicated by the T^{-1} scaling (black solid line).

Assume that R_{ij} has Np eigenvalues significantly larger than $\frac{1}{\alpha}$ and $N(1 - p)$ eigenvalues significantly smaller than $\frac{1}{\alpha}$. These $N(1 - p)$ small eigenvalues become approximately $\frac{1}{\alpha}$ when the regulariser is added, so that the inverse matrix P_{ij} has Np eigenvalues near 0 (which become 1 when multiplied by the large eigenvalues of R_{ij}) and $N(1 - p)$ eigenvalues at α (which vanish when multiplied by the small eigenvalues of R_{ij}). As a result,

$$\int D(t, t') dt = Np. \quad (\text{A10})$$

Appendix B: Relative error scaling with N

To test Eq. (7) on a qualitative level, we perform FORCE learning as described in section VI with $N = 100, 200, 500$, and 1000 , keeping all other parameters the same. The training phase diagrams show that with decreasing N , the success region expands and crosses the instability boundary (Figure 6 a), indicative of a breakdown of the DMFT result. Near the region of $T \approx 25$ and $A \approx 1.5$ the relative error η is observed to be the lowest (Figure 6 a, white rectangles and arrows), and we hypothesise that the η here is most likely to be limited by the finite resolution of the network to learn the target

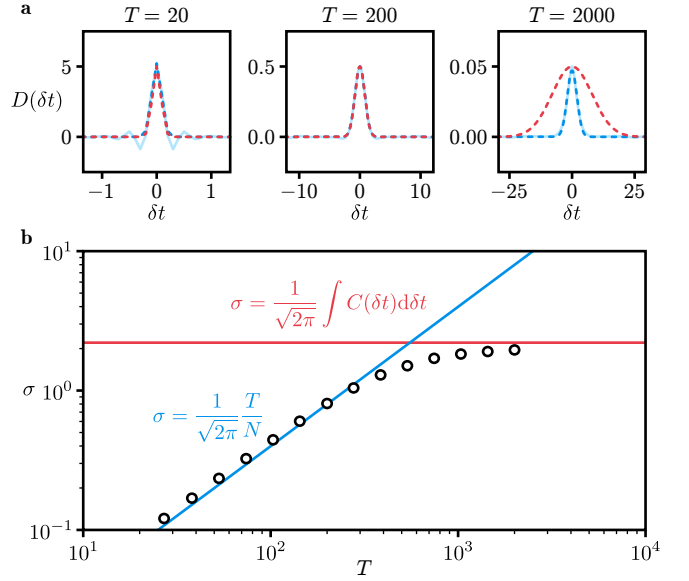


FIG. 5. **Explicit computation of $D(t - t')$.** **a** $D(t - t')$ computed at a range of T (light blue solid lines) give good fits to Gaussians (dark blue dashed lines). The expected peak height is $\frac{N}{T}$, and we plot normalised Gaussians with the same peak value too (red dashed lines). At $T = 20$ and 200 (left and mid), integrals of $D(t - t')$ are normalised to 1 since the Gaussian fits coincide with the normalised Gaussian, but at large T the integral of $D(t - t')$ becomes smaller due to decorrelation. **b** Plotting the standard deviation of the fitted Gaussian (scatter points) shows the expected scaling $\sigma \propto T$ (blue solid line) at small T , but plateaus at higher T (red solid line).

function. We compute η averaged over this small window and plot it as a function of N , and the $\frac{1}{N}$ scaling is observed as predicted by Eq. (7). Note that the η here is computed according to Eq. (17), and the recovered scaling indicates Eq. (17) is closely related to Eq. (7).

Appendix C: Learning a complicated wave

Suppose the target function to be learned is of the form

$$f(t) = A \sum_{n=1}^{\infty} a_n \sin(n\omega t), \quad (\text{C1})$$

for some parameter set a_n , and A now controls the overall amplitude. The mean membrane potential $\bar{h}(t)$ is given by the solution of

$$\frac{d}{dt} \bar{h}(t) = \frac{1}{\tau} \bar{h}(t) + f(t), \quad (\text{C2})$$

and since the equation is linear in $\bar{h}(t)$ we simply get

$$\bar{h}(t) = A \sum_{n=1}^{\infty} \frac{a_n}{\sqrt{1/\tau^2 + n^2\omega^2}} \sin(n\omega t + \theta_n). \quad (\text{C3})$$

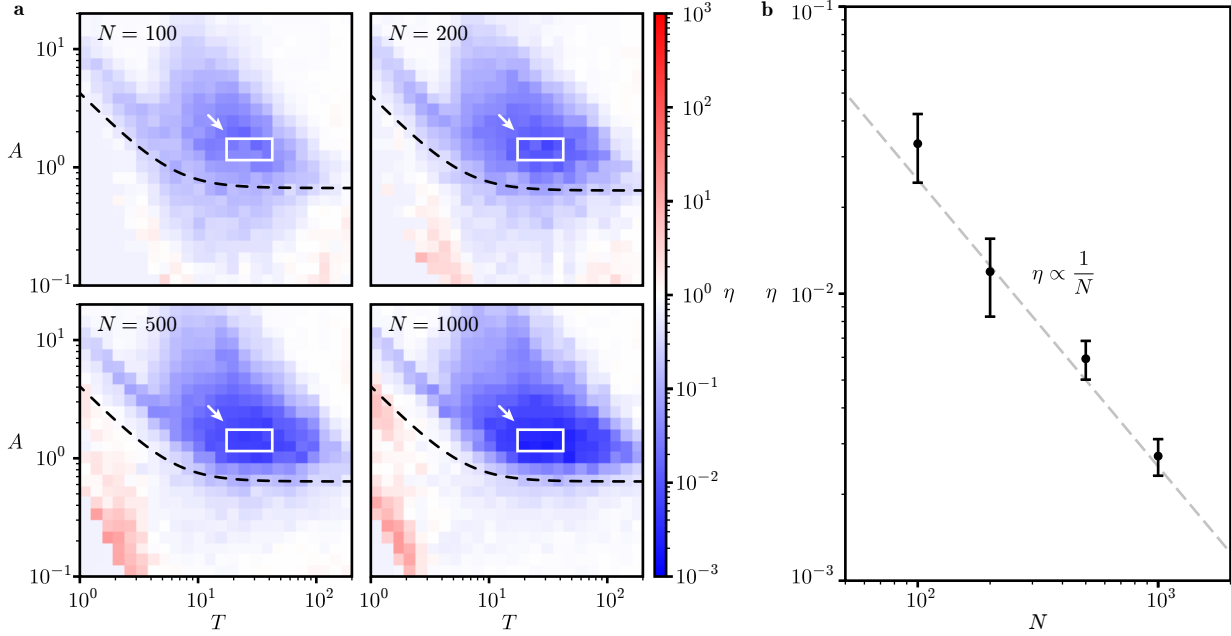


FIG. 6. **Optimal error scaling with N .** **a** Computing FORCE learning phase diagrams for various N shows an increase in the relative error η with decreasing N , and a small A/T window (white rectangles and arrows) is used to compute the minimum η for each N . **b** Plotting η averaged over the selected region as a function of N shows a $\frac{1}{N}$ scaling.

When T is small (ω is large) compared to τ , the $1/\tau^2$ term becomes negligible so we have

$$\begin{aligned} \bar{h}(t) &\approx A \sum_{n=1}^{\infty} \frac{a_n}{n\omega} \sin(n\omega t + \theta_n) \\ &= AT \sum_{n=1}^{\infty} \frac{a_n}{2\pi n} \sin(nt' + \theta_n), \end{aligned} \quad (\text{C4})$$

where $t' \equiv \omega t$ is the dummy integration variable in Eq. (13), and the prefactor AT leads to the overall $A \propto \frac{1}{T}$ scaling.

[1] H. Sompolinsky, A. Crisanti, and H. J. Sommers, “Chaos in random neural networks,” *Physical Review Letters*, vol. 61, no. 3, pp. 259–262, 1988.

[2] D. Paz, “Discontinuous transition to chaos in a canonical random neural network,” no. 2, pp. 1–8, 2024.

[3] W. Maass, T. Natschläger, and H. Markram, “Real-time computing without stable states: A new framework for neural computation based on perturbations,” *Neural Computation*, vol. 14, no. 11, pp. 2531–2560, 2002.

[4] W. Maass, “Liquid state machines: Motivation, theory, and applications,” *Computability in Context: Computation and Logic in the Real World*, pp. 275–296, 2011.

[5] D. Sussillo and L. F. Abbott, “Generating Coherent Patterns of Activity from Chaotic Neural Networks,” *Neuron*, vol. 63, no. 4, pp. 544–557, 2009.

[6] G. Tanaka, T. Yamane, J. B. Héroux, R. Nakane, N. Kanazawa, S. Takeda, H. Numata, D. Nakano, and A. Hirose, “Recent advances in physical reservoir computing: A review,” *Neural Networks*, vol. 115, pp. 100–123, 2019.

[7] J. C. Coulombe, M. C. York, and J. Sylvestre, “Computing with networks of nonlinear mechanical oscillators,” *PLoS ONE*, vol. 12, no. 6, pp. 1–13, 2017.

[8] A. Goudarzi, M. R. Lakin, and D. Stefanovic, “DNA Reservoir Computing: A Novel Molecular Computing Approach,” in *DNA- and RNA-Based Computing Systems*, no. September, pp. 76–89, 2013.

[9] N. Soures, L. Hays, and D. Kudithipudi, “Robustness of a memristor based liquid state machine,” *Proceedings of the International Joint Conference on Neural Networks*, vol. 2017-May, pp. 2414–2420, 2017.

- [10] G. Van Der Sande, D. Brunner, and M. C. Soriano, "Advances in photonic reservoir computing," *Nanophotonics*, vol. 6, no. 3, pp. 561–576, 2017.
- [11] K. Fujii and K. Nakajima, "Harnessing disordered-ensemble quantum dynamics for machine learning," *Physical Review Applied*, vol. 8, no. 2, pp. 2–11, 2017.
- [12] S. S. Haykin, *Adaptive filter theory*. Pearson Education India, aug 2002.
- [13] H. Jaeger, "Adaptive Nonlinear System Identification with Echo State Networks," *NIPS 2002: Proceedings of the 15th International Conference on Neural Information Processing Systems*, pp. 593–600, 2002.
- [14] L. Logiaco, L. F. Abbott, and S. Escola, "Thalamic control of cortical dynamics in a model of flexible motor sequencing," *Cell Reports*, vol. 35, no. 9, p. 109090, 2021.
- [15] K. Rajan, L. F. Abbott, and H. Sompolinsky, "Stimulus-dependent suppression of chaos in recurrent neural networks," *Physical Review E - Statistical, Nonlinear, and Soft Matter Physics*, vol. 82, no. 1, pp. 1–5, 2010.
- [16] T. A. E. Lindell, O. H. Ramstad, I. Sandvig, A. Sandvig, and S. Nichele, "Information encoding and decoding in in-vitro neural networks on micro electrode arrays through stimulation timing," 2024.
- [17] R. Penrose, "A generalized inverse for matrices," *Mathematical Proceedings of the Cambridge Philosophical Society*, vol. 51, no. 3, pp. 406–413, 1955.